



Hierarchical MoS₂/NiCo₂S₄@C urchin-like hollow microspheres for asymmetric supercapacitors

Qinghao Li^{a,1}, Wen Lu^{a,1}, Zhipeng Li^{a,1}, Jiqiang Ning^b, Yijun Zhong^a, Yong Hu^{a,*}

^a Key Laboratory of the Ministry of Education for Advanced Catalysis Materials, Department of Chemistry, Zhejiang Normal University, Jinhua 321004, China

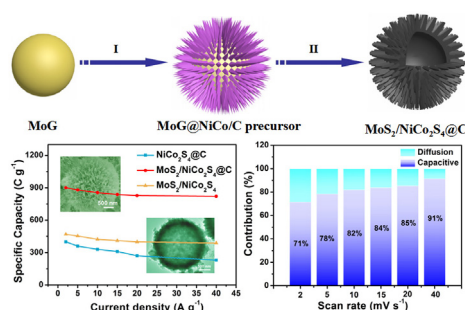
^b Vacuum Interconnected Nanotech Workstation, Suzhou Institute of Nano-Tech and Nano-Bionics, Chinese Academy of Sciences, Suzhou 215123, China



HIGHLIGHTS

- MoS₂/NiCo₂S₄@C HMSs were used as a high-performance supercapacitor.
- MoS₂/NiCo₂S₄@C HMSs were prepared by a facile self-template method.
- The ASCs was assembled with MoS₂/NiCo₂S₄@C HMSs and active carbon.
- The ASCs device exhibits ultra-high rate capability and high-power density.

GRAPHICAL ABSTRACT



ARTICLE INFO

Keywords:

Self-templating synthesis
MoS₂/NiCo₂S₄@C
Hollow hybrid microspheres
Supercapacitors
Ultra-high rate capability

ABSTRACT

Metal sulfides are intensively studied as one of the most predominant materials for supercapacitors owing to such unique advantages as low-cost, low electronegativity and high electrochemical activity, and the appropriate architecture of hybrid metal sulfides is believed to be very effective for fully utilizing their material merits and breaking through their limits of the low-rate capability and inferior cycling stability in supercapacitor applications. Herein, a high-performance supercapacitor based on carbon-coated MoS₂/NiCo₂S₄ urchin-like hollow hybrid microspheres (MoS₂/NiCo₂S₄@C HMSs) is prepared by a facile self-template method. And the high specific capacity of 250 mAh g⁻¹ at 2 A g⁻¹ and ultra-high rate capability of 91.1% at 40 A g⁻¹ achieved with the resultant MoS₂/NiCo₂S₄@C HMSs due to their hierarchical hollow hybrid structure and the protection from the coated carbon thin layer. With the MoS₂/NiCo₂S₄@C HMSs as the positive electrode and active carbon as the negative electrode, asymmetric supercapacitors (ASCs) have been assembled, which exhibit a high energy density of 53.01 Wh kg⁻¹ at the power density of 4.20 kW kg⁻¹, an energy density of 36.46 Wh kg⁻¹ even at the ultra-high power density of 73.75 kW kg⁻¹, and excellent cycling stability of 90.1% after 10 000 cycles of charge-discharge tests at the current density of 10 A g⁻¹.

1. Introduction

To meet the demands of the electronic devices, research efforts are devoted to developing state-of-the-art energy storage devices with high-

energy and high-power densities [1,2]. Due to the fast charge/discharge processes, long cycling life and high power density [3–5], supercapacitors (SCs) have deemed as a promising energy storage device with various electronic applications, such as portable devices, digital

* Corresponding author.

E-mail address: yonghu@zjnu.edu.cn (Y. Hu).

¹ These authors contributed equally to this work.

cameras, all-electric vehicles and roll-up screens. However, their practical applications are usually limited by low energy density [6]. To resolve this problem, an appropriate choice is to construct asymmetric supercapacitors (ASCs) with enhanced specific capacity and extending the cell voltage to boost the energy density without compromising the power density [7].

Currently, transition metal sulfides (TMSs) including CoS_x , NiS_x and CuS_x have been considered as novel cathodes in SCs with enhanced specific capacities, energy and power densities owing to their lower electronegativity and higher electrochemical activity [8]. Especially, binary-TMSs can offer richer redox reactions than mono-TMSs and they show superior specific capacity [9]. However, the relative poor electrical conductivity still hinders their practical applications because of the low rate capability and inferior cycling stability [10,11]. It is promising to introduce a component with good electrical conductivity to form hybrid. The hybrids can not only improve the internal electrical conductivity to facilitate the electron transport at the hetero-phase interfaces, but also can fully utilize the merits of individual component to boost the electrochemical performances by the synergistic effect of individual components [12]. For example, Tan et al. prepared $\text{NiCo}_2\text{S}_4@ \text{MoS}_2$ heterostructures, which exhibits higher rate capability than that of the NiCo_2S_4 electrode [13]. Ma et al. reported the $\text{NiCo}_2\text{S}_4/\text{MoS}_2$ nanotube arrays with higher specific capacity [14]. Despite these advances achieved, it is still a challenge to enhance the cycling stability. As one of the most important carbon-based materials, carbonaceous materials have exhibited the unique merits including high surface area, superior surface wettability and excellent mechanical stability [15]. Specifically, carbonaceous materials can offer continuous pathways for electrons and ions to boost kinetics and prevent the dissolution of active components to achieve superior stability [16,17]. In addition, the carbonaceous materials can play the crucial role as the provider of capacity by surface adsorption/desorption to further improve the specific capacity [18].

Hollow micro-/nanostructures with void interior can greatly enlarge the active surfaces and interfacial contact between electrolyte and electrode materials for fast ions/electrons transport, which benefits for boosting rate capability [19–22]. Moreover, the unique hollow architecture can accommodate the volume expansion during redox processes, resulting in the enhanced stability [22–25]. Therefore, the hierarchical hollow structure is expected to become the superior electrode materials in SCs. Although many efforts have been dedicated to exploring the high-performance SCs, it is still deficient as it requires rational design of advantageous architectures.

Herein, a self-template strategy has been developed to prepare the hierarchical carbon-coated $\text{MoS}_2/\text{NiCo}_2\text{S}_4$ urchin-like hollow hybrid microspheres ($\text{MoS}_2/\text{NiCo}_2\text{S}_4@ \text{C}$ HMSs). Using Molybdenum-Glycerate nanospheres (MoG NSs) as self-template, glucose, $\text{Co}(\text{NO}_3)_2 \cdot 6\text{H}_2\text{O}$ and $\text{Ni}(\text{NO}_3)_2 \cdot 6\text{H}_2\text{O}$ as the raw materials, the hierarchical $\text{MoG}@ \text{NiCo}$ -precursor@C microspheres (MSs) with urchin-like structure are obtained, and then further transformed to $\text{MoS}_2/\text{NiCo}_2\text{S}_4@ \text{C}$ HMSs by a sulfidation reaction of thioacetamide (TAA) in ethanol. Compared with the previously reported work of the $\text{NiCo}_2\text{S}_4\text{-C-MoS}_2$ composite electrodes [26], the as-prepared $\text{MoS}_2/\text{NiCo}_2\text{S}_4@ \text{C}$ HMSs integrate the structural and compositional advantages, including the synergistic binary metal composition, short diffusion paths, abundant active surfaces, which exhibit a higher specific capacity of 250 mAh g^{-1} at 2 A g^{-1} at the current density of 2 A g^{-1} and the ultrahigh rate capability of 91.1% at a current density of 40 A g^{-1} . Meanwhile, it has been found that a thin carbon layer can prevent the aggregation and dissolution of active components, resulting in the enhanced cycling stability. The corresponding ASC is further assembled by using the $\text{MoS}_2/\text{NiCo}_2\text{S}_4@ \text{C}$ HMSs as the positive electrode and active carbon as the negative electrode, which achieves a high energy density of 36.46 Wh kg^{-1} at a ultrahigh power density of 73.75 kW kg^{-1} and excellent cycling stability (90.1% retention after 10 000 cycles). The rational design concept in this work is a versatile path for high-

performance ASCs.

2. Experimental section

2.1. Synthesis of the MoG templates

All reagents were of analytical grade and used as received without further purification. In a typical synthesis, MoG NSs were synthesized through a solvothermal method according to the previous report [27,28]. 90 mg of molybdenyl acetylacetonate and 6 mL of glycerol were added into a mixed solution containing 22.5 mL of isopropanol and 7.5 mL of distilled water. The mixture was sonicated for 40 min to obtain a homogeneous solution, and then transferred into a 50 mL Teflon-lined stainless steel autoclave and heated at 190°C for 3 h. After cooled down to room temperature, the resulting dark brownish precipitate was centrifuged and washed with ethanol for several times, and dried in a vacuum oven at 60°C for overnight.

2.2. Synthesis of $\text{MoS}_2/\text{NiCo}_2\text{S}_4@ \text{C}$ HMSs

20 mg of as-prepared MoG NSs, 1 g of polyvinyl pyrrolidone (PVP, K-30), 291 mg of $\text{Ni}(\text{NO}_3)_2 \cdot 6\text{H}_2\text{O}$, 582 mg of $\text{Co}(\text{NO}_3)_2 \cdot 6\text{H}_2\text{O}$, 600 mg of urea and 180 mg of glucose were added into a mixture containing 20 mL of ethanol and 20 mL of distilled water. After sonicating for 30 min, the mixture was transferred into a 50 mL Teflon-lined stainless steel autoclave and heated at 180°C for 6 h. The resulting $\text{MoG}@ \text{NiCo}$ -precursor@C MSs were collected by centrifugation and washed with water and ethanol for several times.

Then, 20 mg of the as-prepared $\text{MoG}@ \text{NiCo}$ -precursor@C MSs and 120 mg of TAA were dispersed in 40 mL of ethanol/water (V/V = 3:1) mixed solution, which was transferred into a 50 mL Teflon-lined autoclave and heated at 200°C for 4 h. The black product was centrifuged and washed for several times with water and ethanol, and then dried at 60°C overnight. For comparison, the $\text{MoS}_2/\text{NiCo}_2\text{S}_4$ nanoparticles ($\text{MoS}_2/\text{NiCo}_2\text{S}_4$ NPs) were synthesized via the same route without the presence of glucose. Similarly, the $\text{NiCo}_2\text{S}_4@ \text{C}$ NPs were synthesized without the addition of MoG templates. As comparison, the $\text{MoS}_2/\text{NiS}@ \text{C}$ was also synthesized without the presence of $\text{Co}(\text{NO}_3)_2 \cdot 6\text{H}_2\text{O}$ and $\text{MoS}_2/\text{CoS}@ \text{C}$ was synthesized without the addition of $\text{Ni}(\text{NO}_3)_2 \cdot 6\text{H}_2\text{O}$, respectively.

2.3. Materials characterization

The morphology and microstructure of the products were investigated by scanning electron microscopy (SEM) with an accelerating voltage of 5 kV with a Hitachi S-4800 scanning electron micro-analyzer and focused ion beam SEM (FIB-SEM, Zeiss Auriga) with an accelerating voltage of 30 kV. Transmission electron microscopy (TEM), high-resolution TEM (HRTEM) and selected area electron diffraction (SAED) were conducted at 200 kV with a JEM-2100F field emission TEM. The crystallinity of the samples was characterized by powder X-ray diffraction (XRD) on a Philips PW3040/60 X-ray diffractometer using Cu-K α radiation at a scanning rate of $0.06^\circ \text{ s}^{-1}$. X-ray photoelectron spectroscopy (XPS) measurements were performed using an ESCALab MKII X-ray photoelectron spectrometer with Al K α X-ray radiation. N_2 adsorption isotherms were obtained at 77 K on a Micrometrics ASAP 2020 surface area and porosity analyzer after the sample was degassed in vacuum at 150°C for 3 h. Raman spectroscopy was performed using a Renishaw inVia-Reflex and 532 nm laser excitation with working distances on a $50 \times$ lens. The thermogravimetric analysis (TGA) of the product was performed on a Netzsch STA 449C thermal analyzer.

2.4. Electrochemical measurements

The working electrodes were prepared as follows, the as-obtained active materials, carbon black and poly(vinylidene fluoride) (PVDF)

with a mass ratio of 8:1:1 were dispersed in N-methylpyrrolidone (NMP) to form homogeneous slurry. Then, the slurry was pressed onto a nickel foam and was dried at 80 °C for 12 h. The mass loading of the activate materials was about 1.5 mg cm⁻².

All the tests including cyclic voltammetry (CV), galvanostatic charge–discharge (GCD) and electrochemical impedance spectroscopy (EIS) were conducted on a Zennium E (Zahner, Germany) electrochemical workstation. To investigate the electrochemical performance, the MoS₂/NiCo₂S₄@C HMSs, MoS₂/NiCo₂S₄ NPs and NiCo₂S₄@C NPs electrode were explored under a three-electrode configuration using Hg/HgO electrode as reference electrode and Pt foil as a counter electrode in 6.0 M KOH aqueous solution at room temperature. EIS measurements were performed by employing an AC voltage with 5 mV amplitude in the frequency range of 10 mHz to 100 kHz at open circuit potential. From the CV curves, specific capacitance C_{s1} (F g⁻¹) of the electrode materials was calculated by integrating the discharge portion using the following equation:

$$C_{s1} = \frac{\int IdV}{vmV} \quad (1)$$

where I is current (A), v is the scan rate (V s⁻¹), m is the mass of the active material (g), and V is the potential window (V), respectively.

The specific capacitance (C_{s2} , F g⁻¹) was calculated from the galvanostatic discharge curves according to the following formulas:

$$C_{s2} = (I \times \Delta t) / (m \times \Delta V) \quad (2)$$

where I is the discharge current (A), Δt is the discharge time (s), ΔV is the voltage (V) range upon discharging and m is the mass (g) of the active material. And the specific capacity (mAh g⁻¹) was accordingly deduced from the following equation [29]

$$Q = C \times V / 3.6 \quad (3)$$

2.5. Assembly of ASCs

The as-prepared electrodes were assembled into a button-type supercapacitor by using MoS₂/NiCo₂S₄@C HMSs as the positive electrode, active carbon (AC) as the negative electrode and one piece of cellulose paper as the separator in 6.0 M KOH electrolyte. The negative electrode was prepared by casting the mixture which contains AC, carbon black and PVDF with a weight ratio of 8:1:1 onto nickel foam. The mass ratio of the MoS₂/NiCo₂S₄@C HMSs to AC was determined to be approximately 0.13, which can obtain the charge balance between the two electrodes according to the following equation (3):

$$\frac{m_+}{m_-} = \frac{C_- \Delta V_-}{C_+ \Delta V_+} \quad (4)$$

where C is the specific capacitance (F g⁻¹), m is the mass of active material (g) and ΔV is the potential (V) window range for positive and negative electrodes, respectively. The energy density (E , Wh kg⁻¹) and power density (P , W kg⁻¹) of the device are calculated according to the following formulas:

$$E = \frac{\int i V dt}{M \times 3.6} \quad (5)$$

$$P = \frac{E}{t} \times 3600 \quad (6)$$

where C is the cell capacitance (F g⁻¹), ΔV is the voltage (V) range during the charge-discharge measurement and Δt is the discharge time (s).

3. Results and discussion

The formation of the hierarchical MoS₂/NiCo₂S₄@C HMSs is schematically presented in Fig. 1. The uniform MoG NSs are employed as

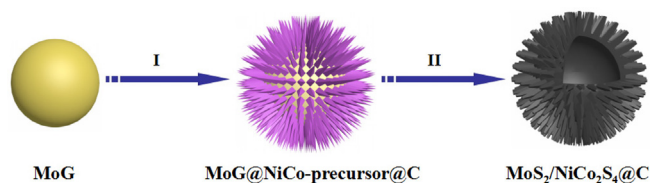


Fig. 1. Schematic formation of MoS₂/NiCo₂S₄@C HMSs.

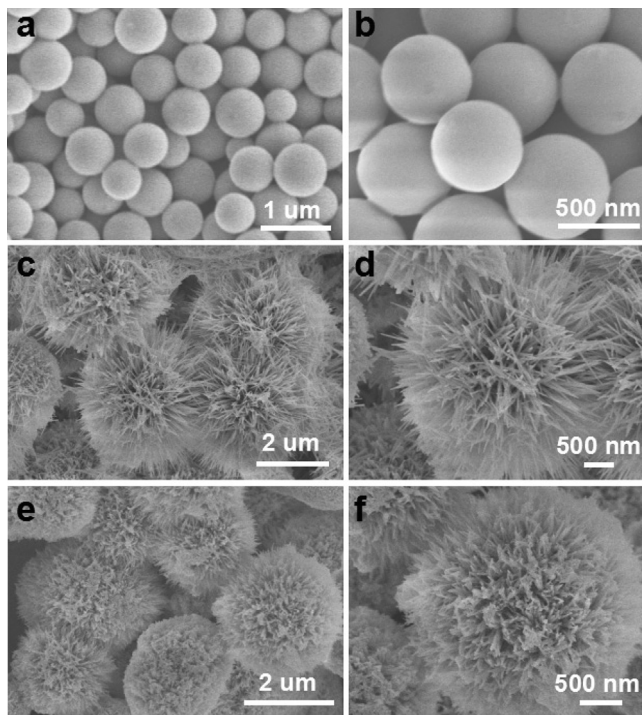


Fig. 2. SEM images of the as-prepared (a, b) MoG NSs, (c, d) MoG@NiCo-precursor@C MSs, (e, f) MoS₂/NiCo₂S₄@C HMSs.

self-template to construct urchin-like hierarchical MoG@NiCo-precursor@C MSs in the ethanol/water mixed solution containing glucose, Co(NO₃)₂·6H₂O, Ni(NO₃)₂·6H₂O, PVP and urea at 180 °C for 6 h. After sulfidation, the urchin-like MoG@NiCo-precursor@C MSs are successfully converted into the hierarchical MoS₂/NiCo₂S₄@C HMSs by a facile anion-exchange reaction at 200 °C for 4 h.

The morphology and the structure of the as-prepared samples were characterized by SEM. As displayed in Fig. 2a, b, the MoG product consists entirely of uniformly smooth nanospheres with an average diameter of around 500 nm. After the chemical reaction in step I, the MoG NSs are completely converted into hierarchical MoG@NiCo-precursor@C MSs with obvious urchin-like structure (Fig. 2c, d). As shown in Fig. S1, the corresponding XRD pattern indicates the formation of Ni₂CO₃(OH)₂·H₂O (JCPDS No. 29-0868) and Co(CO₃)_{0.5}(OH)·0.11H₂O (JCPDS No. 48-0083) hybrid. Obviously, numerous NiCo-precursor needles are vertically attached to the surface of MoG NSs. In the following sulfidation process, the as-prepared MSs are transformed to MoS₂/NiCo₂S₄@C HMSs with the well retained urchin-like structure and the rougher surface can be observed (Fig. 2e, f). For comparison, the MoS₂/NiS@C MSs and MoS₂/CoS@C MSs are also synthesized, which exhibit the similar microsphere structure with rough surface (Fig. S2). It is noteworthy that the presence of MoG NSs and glucose in the reaction process plays a vital role in the formation of the hierarchical hollow hybrid microspheres morphology. Without the presence of MoG NSs or glucose, the resulting NiCo₂S₄@C and MoS₂/NiCo₂S₄ samples both exhibit irregular aggregates of nanoparticles, as shown in Fig. S3. During the evolution of the hierarchical urchin-like hollow

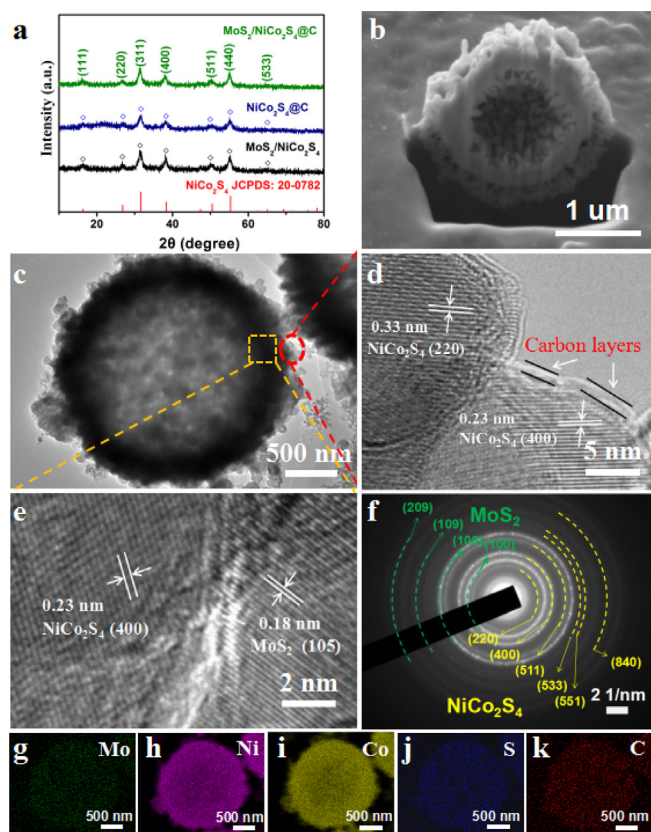


Fig. 3. (a) XRD patterns of the as-prepared $\text{MoS}_2/\text{NiCo}_2\text{S}_4@\text{C}$ HMSs, $\text{NiCo}_2\text{S}_4@\text{C}$ and $\text{MoS}_2/\text{NiCo}_2\text{S}_4$ NPs, respectively, (b) FIB-SEM image, (c) TEM image, (d–e) HRTEM images, (f) SAED pattern of the as-prepared $\text{MoS}_2/\text{NiCo}_2\text{S}_4@\text{C}$ HMSs and corresponding elemental mapping images of (g) Mo, (h) Ni, (i) Co, (j) S and (k) C.

microspheres, the MoG NSs are employed as self-template to provide a center to support the growth of NiCo-precursor needles, and a thin carbon layer obtained from glucose can maintain the pristine sphere morphology. Additionally, N_2 adsorption-desorption tests were examined to further confirm the surface area and porous structure of the as-prepared samples. As displayed in Fig. S4, the $\text{MoS}_2/\text{NiCo}_2\text{S}_4@\text{C}$ HMSs exhibit a relatively high Brunauer–Emmett–Teller (BET) surface area of $100.31 \text{ m}^2 \text{ g}^{-1}$ with an average pore size of 2.8 nm, while the BET surface area of the $\text{NiCo}_2\text{S}_4@\text{C}$ NPs and $\text{MoS}_2/\text{NiCo}_2\text{S}_4$ NPs is examined to be $31.23 \text{ m}^2 \text{ g}^{-1}$ and $32.59 \text{ m}^2 \text{ g}^{-1}$, respectively. This result indicates the as-prepared $\text{MoS}_2/\text{NiCo}_2\text{S}_4@\text{C}$ HMSs can provide more electroactive sites to boost the electrochemical performance.

The XRD patterns of the as-prepared $\text{MoS}_2/\text{NiCo}_2\text{S}_4@\text{C}$ HMSs, $\text{NiCo}_2\text{S}_4@\text{C}$ NPs and $\text{MoS}_2/\text{NiCo}_2\text{S}_4$ NPs, as displayed in Fig. 3a, manifest that all the diffraction peaks can be well indexed to the cubic NiCo_2S_4 (JCPDS No. 20-0782). However, no typical diffraction peaks of MoS_2 can be found, indicating that the content of MoS_2 is below the detection limit of XRD. It is well-known that MoS_2 possesses two typical crystal structures of 2H semiconductor phase and 1T metallic phase [30,31]. Raman spectroscopy was further used to analyze the MoS_2 phase. As shown in Fig. S5, the peaks at 151, 236, 339, 380 and 406 cm^{-1} are the feature vibrations of 1T metallic phase of MoS_2 , indicating that the high electrical conductivity can be obtained in this system. In addition, the TGA test exhibits the mass ratio of carbon content in the as-prepared sample is about 7.6% (Fig. S6) [32]. From the FIB-SEM image of the as-obtained $\text{MoS}_2/\text{NiCo}_2\text{S}_4@\text{C}$ sample in Fig. 3b, the void interior can be obviously observed, exhibiting the successfully formation of hollow structure in the final product. The TEM image (Fig. 3c) further elucidates the hollow nature of the $\text{MoS}_2/$

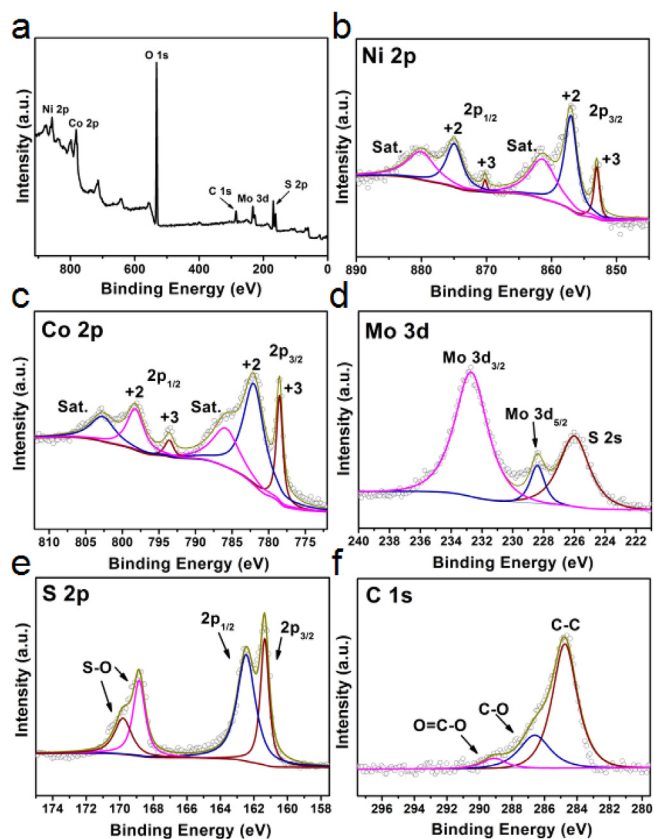


Fig. 4. XPS spectra of the as-prepared $\text{MoS}_2/\text{NiCo}_2\text{S}_4@\text{C}$ HMSs. (a) survey spectrum and the high resolution XPS spectra of (b) Ni 2p, (c) Co 2p, (d) Mo 3d, (e) S 2p and (f) C 1s.

$\text{NiCo}_2\text{S}_4@\text{C}$ HMSs by the sharp contrast between the center and the edge. The hollow architecture endows the sample with a highly active surfaces, resulting in enhanced electrochemical performances. The HRTEM images (Fig. 3d, e) show lattice fringe spacing of 0.23, 0.33 and 0.18 nm corresponding to the (400) and (220) plane of the NiCo_2S_4 and the (105) plane of MoS_2 , respectively. Furthermore, a thin amorphous carbon layer can be obviously observed at the edge of sample, as displayed in Fig. 3d. This unique architecture ensures the structural integrity, which boosts the long-term stability. In addition, the SAED pattern (Fig. 3f) reveals that a series of diffraction rings are assigned to different diffraction planes of crystalline NiCo_2S_4 and MoS_2 , which also indicates the existence of MoS_2 . The multicomponent sulfides of the products are performed by EDX mapping (Fig. 3g–k), which confirms that Mo, Ni, Co, S and C elements are homogeneously distributed throughout the whole hollow microspheres, further revealing the existence of the C and MoS_2 rather than pure NiCo_2S_4 .

The elemental composition and chemical states of the as-prepared $\text{MoS}_2/\text{NiCo}_2\text{S}_4@\text{C}$ HMSs were performed by XPS. The survey spectrum (Fig. 4a) and Table S1 reveal the existence and the atomic percentages of Ni, Co, Mo, C and S elements in the hierarchical $\text{MoS}_2/\text{NiCo}_2\text{S}_4@\text{C}$ HMSs, respectively. The high-resolution XPS spectrum (Fig. 4b) of Ni 2p shows the peaks with the binding energies of 853.0 eV in $\text{Ni } 2p_{3/2}$ and 870.2 eV in $\text{Ni } 2p_{1/2}$ belong to Ni^{3+} , while the peaks at 857.0 eV and 874.9 eV correspond to $\text{Ni}^{2+} 2p_{3/2}$ and $\text{Ni}^{2+} 2p_{1/2}$, respectively [33,34]. In the Co 2p spectrum (Fig. 4c), the peaks at 778.5/782.0 eV and 793.6/798.2 eV are assigned to the Co $2p_{3/2}$ and Co $2p_{1/2}$, respectively, confirming the formation of Co^{3+} and Co^{2+} [35–37]. In Fig. 4d, the peaks located at 228.4 and 232.4 eV are considered as the characteristic peaks of MoS_2 , which correspond to Mo $3d_{5/2}$ and Mo $3d_{3/2}$, respectively [38]. Furthermore, the binding energy at 226.5 eV can be attributed to S 2s from MoS_2 . As presented in Fig. 4e, the S $2p_{3/2}$

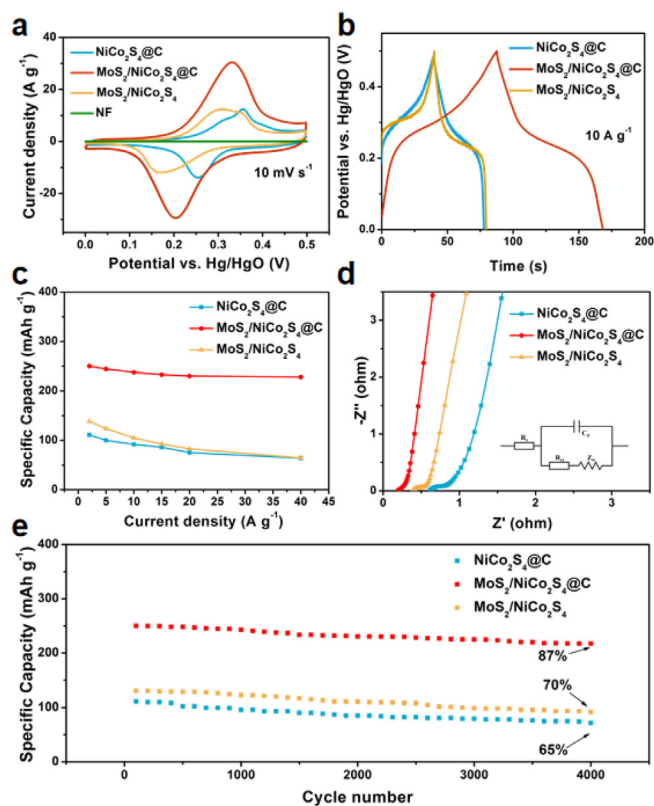


Fig. 5. (a) CV curves of the as-prepared Ni foam, MoS₂/NiCo₂S₄@C HMSs, NiCo₂S₄@C NPs, MoS₂/NiCo₂S₄ NPs electrodes at 10 mV s⁻¹. (b) Galvanostatic charge–discharge (GCD) curves of the as-prepared MoS₂/NiCo₂S₄@C HMSs, NiCo₂S₄@C NPs, MoS₂/NiCo₂S₄ NPs electrodes at 10 A g⁻¹. (c) Specific capacities of the as-prepared MoS₂/NiCo₂S₄@C HMSs, NiCo₂S₄@C NPs, MoS₂/NiCo₂S₄ NPs electrodes at different current densities. (d) Nyquist plots of the as-prepared MoS₂/NiCo₂S₄@C HMSs, NiCo₂S₄@C NPs, MoS₂/NiCo₂S₄ NPs electrodes. (e) Cycling stability of the as-prepared MoS₂/NiCo₂S₄@C HMSs, NiCo₂S₄@C NPs, MoS₂/NiCo₂S₄ NPs electrodes at 10 A g⁻¹.

and 2p_{1/2} with binding energies at 161.7 and 162.9 eV are ascribed to the S²⁻, and other peaks at 169.0 eV can be attributed to the oxidized state S on the surface of the material [38,39]. Fig. 4f displays the peaks located at 284.8, 286.6 eV and 289.1 eV belong to C–C, C–O and O=C–O, respectively [40,41]. The XPS results further verify the existence of carbonaceous layer in the MoS₂/NiCo₂S₄@C HMSs.

The electrochemical properties of MoS₂/NiCo₂S₄@C HMSs, MoS₂/NiCo₂S₄ NPs and NiCo₂S₄@C NPs electrodes were evaluated by a three-electrode system with Pt foil as a counter electrode and Hg/HgO as a reference electrode in a 6 M KOH aqueous electrolyte. From the CV curves (Fig. 5a), the three electrodes all exhibit a pair of redox peaks in each curve at a scan rate of 10 mV s⁻¹ with a potential window of 0–0.5 V, which can be ascribed to the reversible Faradaic reaction in the alkaline electrolyte. And it is evident that the bare Ni foam (NF) displays a negligible contribution to the entire electrode capacity in the CV test. Among the three electrodes, the integral area of MoS₂/NiCo₂S₄@C HMSs is much larger than those of the as-prepared MoS₂/NiCo₂S₄ and NiCo₂S₄@C NPs, indicating the enhanced specific capacity, which can be attributed to the hollow architecture and the synergistic effect. The hollow architecture can provide more electroactive sites and enhanced interfacial contact between electrode and electrolyte. Meanwhile, the MoS₂ can accelerate the electrical conductivity to facilitate the redox reactions and the protected carbon thin layer can contribute additional specific capacity. This is further confirmed by the GCD at 10 A g⁻¹, as shown in Fig. 5b. Among all the samples, the discharging time of the MoS₂/NiCo₂S₄@C HMSs is the longest, which is in agreement with the CV curves. The detailed CV and GCD curves of MoS₂/NiCo₂S₄@C HMSs,

NiCo₂S₄@C NPs, and MoS₂/NiCo₂S₄ NPs are presented in Fig. S7 and the corresponding specific capacities are demonstrated in Figs. S8 and 5c, respectively. It can be seen that the MoS₂/NiCo₂S₄@C HMSs electrode exhibits the highest specific capacity of 250 mAh g⁻¹ at 2 A g⁻¹, which is 1.8 times and 2 times larger than the MoS₂/NiCo₂S₄ NPs and NiCo₂S₄@C NPs, respectively. According to the CV curves, the MoS₂/NiCo₂S₄@C HMSs electrode displays the specific capacity of 268 mAh g⁻¹ at 2 mV s⁻¹, whereas only 114 and 141 mAh g⁻¹ are obtained for NiCo₂S₄@C and MoS₂/NiCo₂S₄ samples, respectively. The calculated specific capacities based on the GCD curves for the MoS₂/NiCo₂S₄@C HMSs electrode are 250, 244, 238, 233, 230 and 228 mAh g⁻¹ at the current density of 2, 5, 10, 15, 20 and 40 A g⁻¹, respectively. With the increased current densities, the specific capacities exhibit the decreasing trend, which is associated with the shortened time for redox process. Significantly, the MoS₂/NiCo₂S₄@C HMSs electrode retains ultrahigh rate capability of 91.1% when the current density is increased from 2 to 40 A g⁻¹, which is also superior than that of reported Ni-Co-Mo-S based electrode materials (Table S2). This ultrahigh rate capability is attributed to the enhanced electrical conductivity caused by the presence of the MoS₂ and the protected thin carbon layer. The coulombic efficiency is calculated with the following equation:

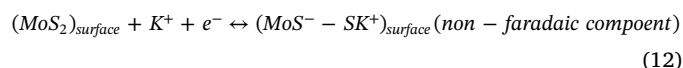
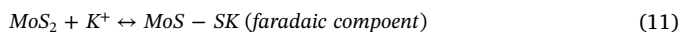
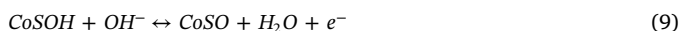
$$\eta = \frac{t_d}{t_c} \quad (7)$$

where t_c and t_d are the charging and discharging time, respectively. The coulombic efficiency of the as-prepared MoS₂/NiCo₂S₄@C electrode at low current density is inferior to the high current density, which is due to the side effect (Fig. S9) [42,43]. To investigate the synergistic effect between Co and Ni ions in the final product, the electrochemical performances of the as-prepared MoS₂/NiS@C and MoS₂/CoS@C samples are shown in Fig. S10. From the CV curves, the two electrodes all exhibit a pair of redox peaks. According to the GCD curves, the specific capacities are calculated (Fig. S10e). Obviously, the specific capacities of the MoS₂/NiS@C electrode are higher than the MoS₂/CoS@C electrode, but the rate capability of the MoS₂/CoS@C electrode is superior to the MoS₂/NiS@C electrode. It can be concluded that the Ni ions show higher electrochemical activity than Co ions and Co ions contribute to higher rate performance [44]. Integrating the advantages of the Ni and Co ions, the MoS₂/NiCo₂S₄@C HMSs show the highest specific capacity and excellent rate capability, verifying that the synergistic effect between Ni, Co improves the electrochemical performance.

The electrochemical impedance spectroscopy (EIS) measurements were investigated to further gain the intrinsic electrochemical and kinetic mechanisms. The Nyquist plots are presented in Fig. 5d. The intercept of the X-axis in the high-frequency region represents the equivalent series resistance (R_s), including the intrinsic resistance, electrolyte resistance and contact resistance between the electrode and current collector. Remarkably, the MoS₂/NiCo₂S₄@C HMSs exhibit a lower R_s of 0.17 Ω than that of MoS₂/NiCo₂S₄ NPs (R_s = 0.37 Ω) and NiCo₂S₄@C NPs (R_s = 0.61 Ω). In addition, the diameter of the semi-circle indicates charge transfer resistance (R_{ct}) in the high-frequency region and the slope of the straight line in the low-frequency region implies the diffusion resistance (R_w). As expected, the MoS₂/NiCo₂S₄@C HMSs also demonstrate the smallest charge transfer resistance (R_{ct}) of 0.09 Ω (0.2 Ω for MoS₂/NiCo₂S₄ NPs and 0.28 Ω for NiCo₂S₄@C NPs), implying the higher electron transportation kinetics. According to the slope of the straight line, the MoS₂/NiCo₂S₄@C HMSs electrode exhibits more vertical line than the others, which may facilitate ion diffusion. From the Bode plots (Fig. S11), the corresponding characteristic relaxation time constant τ₀ (τ₀ = 1/f₀, the inverse of the characteristic frequency at -45°) is 2018, 691 and 329 ms for the NiCo₂S₄@C, MoS₂/NiCo₂S₄ and MoS₂/NiCo₂S₄@C samples, respectively, indicating the high-speed ion diffusion and transport behavior of the as-prepared MoS₂/NiCo₂S₄@C HMSs, which is in a good agreement with the Nyquist plots. It is worth mentioning that a thin carbon layer can serve as bridges to connect and link all the urchin-like microspheres to

boost the electrical conductivity. Meanwhile, the hierarchical urchin-like hollow structure can efficiently shorten the diffusion paths for electrons and ions. In addition, the cycling stability is another essential factor for practical energy storage devices. Impressively, there is no significant capacity decay after 4000 cycles at a current density of 10 A g^{-1} for the $\text{MoS}_2/\text{NiCo}_2\text{S}_4@\text{C}$ HMSs, maintaining 87.0% of the initial capacity, while the $\text{MoS}_2/\text{NiCo}_2\text{S}_4$ NPs and $\text{NiCo}_2\text{S}_4@\text{C}$ NPs electrodes suffer from 30% and 35% capacity loss, respectively, during the long cycle life (Fig. 5e). The excellent cycling stability can be further verified by the EIS measurements before and after 4000 GCD cycles (Fig. S12), which exhibits slightly increased resistance ($R_s = 0.59 \Omega$; $R_{ct} = 0.72 \Omega$) after the 4000th cycles. To further prove the structural stability of the as-prepared sample, the $\text{MoS}_2/\text{NiCo}_2\text{S}_4@\text{C}$ electrode after long-term cyclic stability test is characterized by SEM. The morphology of the $\text{MoS}_2/\text{NiCo}_2\text{S}_4@\text{C}$ is not greatly affected after the cycling tests, demonstrating a good structural stability (Fig. S13). These above results confirm that the unique hollow architectures and the compositions are accountable for the enhanced electrochemical performances. In particular, the hollow structure can serve as electrolyte reservoirs and the thin carbon layer coated on the $\text{MoS}_2/\text{NiCo}_2\text{S}_4$ can efficiently inhibit the disintegration of the electrode, resulting in enhanced durability of electrodes.

The CV curves of the $\text{MoS}_2/\text{NiCo}_2\text{S}_4@\text{C}$ HMSs electrode at various scan rates ranging from 2 to 40 mV s^{-1} are presented in Fig. 6a. A pair of redox peaks are observed in each CV curve, indicating the reversible faradaic reaction of $\text{MoS}_2/\text{NiCo}_2\text{S}_4@\text{C}$ HMSs electrode in the electrochemical process. The energy storage mechanism is involved with the following reversible redox reactions [45–47]:



In order to further investigate the capacitive contribution of $\text{MoS}_2/\text{NiCo}_2\text{S}_4@\text{C}$ HMSs, we analyze the relationship between current (i) and scan rate (v) according to the power law as follows [48]:

$$i = av^b \quad (13)$$

The current (i) obeys the power law relationship with scan rate (v) where the value of b is determined from the slope of $\log(i)$ versus $\log(v)$ plot. The b value of 1 indicates the capacitive process, whereas the b value of 0.5 reflects diffusion controlled process. As shown in Fig. 6b, the calculated b values are 0.74 and 0.86 for the anodic and cathodic peaks, respectively, suggesting the co-existence of diffusion controlled process and capacitive process for the energy storage in the electrode reaction [49–51]. Compared with other diffusion-controlled electrode materials, $\text{MoS}_2/\text{NiCo}_2\text{S}_4@\text{C}$ HMSs deliver ultrahigh rate capability, benefiting from the surface-controlled capacitive process [52].

Quantification of the capacitive contribution to the total capacity is analyzed on the basis of following equation [53]:

$$i(V) = k_1v + k_2v^{1/2} \quad (14)$$

where the $i(V)$ is the total current at a constant potential V , the k_1v and $k_2v^{1/2}$ are the current which result from the capacitive effects and diffusion-controlled process, respectively. Fig. 6c shows that 78% of the entire capacity was identified as the capacitive contribution in a typical CV curve at 5 mV s^{-1} . With the scan rate increased from 2 mV s^{-1} to 40 mV s^{-1} , the capacitive contribution reaches the maximum value of 91% (Fig. 6d), due to the decreasing time for the ion diffusion into the lattices. As a result, the $\text{MoS}_2/\text{NiCo}_2\text{S}_4@\text{C}$ HMSs remain superior specific capacity at the higher scan rate, indicating that the carbon layers provide more efficient pathways for electrons to the $\text{MoS}_2/\text{NiCo}_2\text{S}_4$ surface sites [52].

Based on the above results, the superior electrochemical performances of the as-obtained $\text{MoS}_2/\text{NiCo}_2\text{S}_4@\text{C}$ HMSs are ascribed to the following characteristics: Firstly, the hollow urchin-like hierarchical

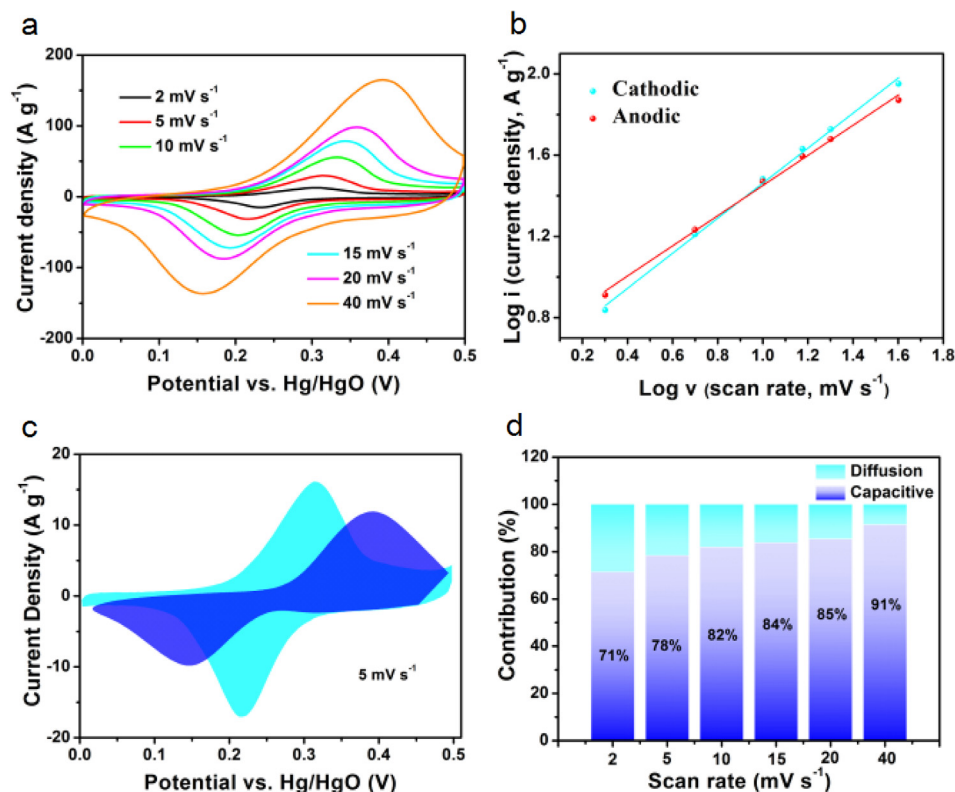


Fig. 6. (a) The CV curves of the as-prepared $\text{MoS}_2/\text{NiCo}_2\text{S}_4@\text{C}$ HMSs electrode at different scan rates. (b) The plot of $\log(i)$ versus $\log(v)$. (c) Separation of the capacitive and diffusion currents in the as-prepared $\text{MoS}_2/\text{NiCo}_2\text{S}_4@\text{C}$ HMSs electrode at 5 mV s^{-1} . (d) Relative contribution of the capacitive and diffusion-controlled charge storage at different scan rates.

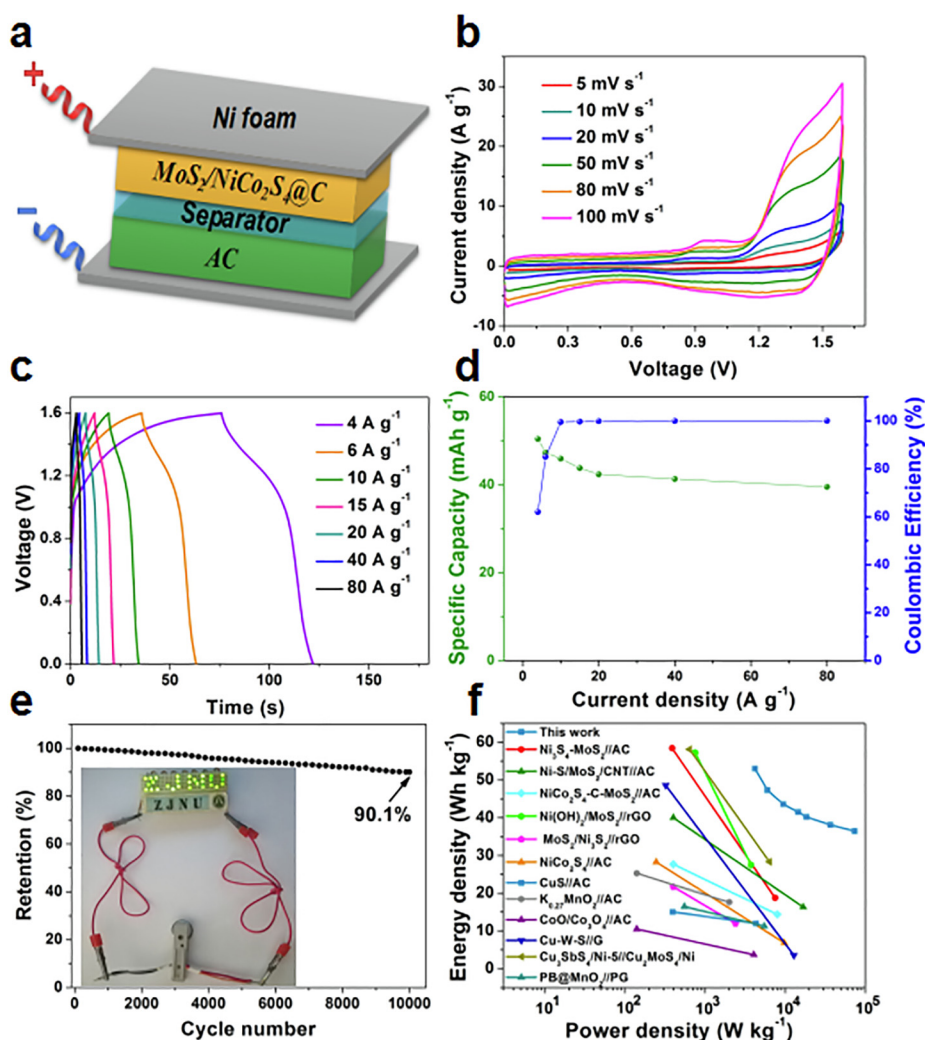


Fig. 7. Electrochemical performances of the as-prepared $\text{MoS}_2/\text{NiCo}_2\text{S}_4@\text{C}/\text{AC}$ ASCs. (a) Schematic illustration of the fabricated ASCs. (b) CV curves at different scan rates, (c) GCD curves at different current densities. (d) Specific capacities and coulombic efficiency at different current densities. (e) Cycling stability at 10 A g^{-1} and the inset in panel shows the LED lights powered by two ASCs in series. (f) The Ragone plot related to energy and power densities.

structure endows the electrode material with a large interfacial contact between the electrode and electrolyte which facilitate the transportation of the ions and electrons. And the void interior can buffer the volume expansion and mechanical strain to enhance the cycling stability. Secondly, the multi-metal sulfides provide richer redox reactions, resulting in superior specific capacity. Thirdly, the electronic conductivity of the resultant hybrid is better than that of mono-component, resulting in ultrahigh rate capability. Fourthly, the protected thin carbon layer can prevent the detachment, aggregation, and pulverization of active components to obtain prominent cycling stability.

In order to further evaluate the $\text{MoS}_2/\text{NiCo}_2\text{S}_4@\text{C}$ HMSs electrode for practical applications, ASC device using $\text{MoS}_2/\text{NiCo}_2\text{S}_4@\text{C}$ HMSs as the positive electrode and AC as the negative electrode is fabricated as schematically shown in Fig. 7a. The CV and GCD curves of the AC electrode are displayed in Fig. S14, which demonstrate the specific capacitance of 120 F g^{-1} at 1 A g^{-1} . As shown in Fig. 7b, the CV curves at different scan rates are presented with the working voltage window ranging from 0 to 1.6 V, which demonstrate the well-distinct redox peaks and remain the characteristics with the scan rate rising to 100 mV s^{-1} , suggesting the exceptional reversibility and fast electron transport kinetics. The corresponding GCD curves at various current densities displayed in Fig. 7c are nonlinear, which is consistent with the CV curves. According to the CV and GCD curves, the calculated specific capacities are presented in Figs. S15 and 7d, respectively. From the CV

curves, it exhibits a highest specific capacity of 67 mAh g^{-1} at 2 mV s^{-1} . Based on the GCD curves, the specific capacities of the ASC are estimated to be 50.44, 47.33, 45.97, 43.79, 42.39, 41.33, 39.56 mAh g^{-1} at current density of 4, 6, 10, 15, 20, 40 and 80 A g^{-1} , respectively, implying the excellent rate capability (Fig. 7d). The specific capacities at high current densities are comparable to recently reported hybrid Na-ion capacitors (28.1 mAh g^{-1} at 30 A g^{-1}) [54]. Additionally, the calculated coulombic efficiency is shown in Fig. 7d. Although the coulombic efficiency is poor at low current density, the asymmetric device exhibits high coulombic efficiency when the current density is increased. A low coulombic efficiency may be attributed to the charge leakage occurring at lower current density [42,55]. To better evaluate the electrode kinetics, EIS measurements are investigated, and the results are shown in Fig. S16. The resistance (R_s) value of 1.06Ω and the R_{ct} is 1.39Ω for ASC prove the outstanding electrical conductivity of electrode. In addition, the cycling stability is one of the critical aspects to determine the feasibility of the energy storage. Remarkably, the ASCs can retain 90.1% of the initial capacity after 10 000 cycles at 10 A g^{-1} , indicating the outstanding stability (Fig. 7e), which benefit from the engineered hierarchical structure and the unique composition. Moreover, as the energy storage devices, the practical application of the ASCs were fully explored. The arranged as “ZJNU” can be easily lit up by two ASCs in series (in the inset of Fig. 7e). The energy density and the power density are two significant factors for the

evaluation of ASCs, which can be calculated based on the GCD curves (Fig. 7f). More significantly, the energy density of our ASC device exhibits 53.01 Wh kg⁻¹ at a power density of 4.20 kW kg⁻¹ and even maintains 36.46 Wh kg⁻¹ at the ultrahigh power density of 73.75 kW kg⁻¹, which is comparable to those of recently reports, such as Ni₃S₄-MoS₂//AC (18.75 Wh kg⁻¹ at 7.5 kW kg⁻¹) [56], Ni-S/MoS₂/CNT//AC (16.3 Wh kg⁻¹ at 16.8 kW kg⁻¹) [57], NiCo₂S₄-C-MoS₂//AC (14.4 Wh kg⁻¹ at 8 kW kg⁻¹) [26], Ni(OH)₂/MoS₂//rGO (27.5 Wh kg⁻¹ at 3.75 kW kg⁻¹) [58], MoS₂/Ni₃S₂//rGO (12 Wh kg⁻¹ at 2.4 kW kg⁻¹) [59], NiCo₂S₄//AC (6.8 Wh kg⁻¹ at 9.8 kW kg⁻¹) [60], CuS//AC (12 Wh kg⁻¹ at 4.32 kW kg⁻¹) [61], K_{0.27}MnO₂·0.6H₂O//AC (17.6 Wh kg⁻¹ at 2.0 kW kg⁻¹) [62], CoO/Co₃O₄//AC (3.72 Wh kg⁻¹ at 4.06 kW kg⁻¹) [63], Cu-W-S//Graphene (3.57 Wh kg⁻¹ at 12.86 kW kg⁻¹) [64], Cu₃SbS₄/Ni-S//Cu₂MoS₄/Ni (28.33 Wh kg⁻¹ at 6.36 kW kg⁻¹) [65], PB@MnO₂//PG (11.3 Wh kg⁻¹ at 5.5 kW kg⁻¹) [66] (Table S3). These results indicate that the ASCs have bright future for energy storage.

4. Conclusions

In summary, we have successfully fabricated a hierarchical MoS₂/NiCo₂S₄@C HMSs through a self-template strategy. Benefiting from the unique structural and compositional advantages, the MoS₂/NiCo₂S₄@C HMSs electrode delivers a higher specific capacity of 250 mAh g⁻¹ at the current density of 2 A g⁻¹, which is 1.8 times and 2 times larger than the MoS₂/NiCo₂S₄ NPs and NiCo₂S₄@C NPs, respectively. In addition, the MoS₂/NiCo₂S₄@C HMSs electrode also exhibits the ultrahigh rate capability of 91.1% at a current density from 2 to 40 A g⁻¹ and superior stability with 87% of the initial capacity after 4000 continuous cycles at the current density of 10 A g⁻¹. The ASC device comprising MoS₂/NiCo₂S₄@C HMSs and AC electrodes achieves an excellent energy density of 53.01 Wh kg⁻¹ at a power density of 4.20 kW kg⁻¹ and even retains 36.46 Wh kg⁻¹ at the ultrahigh power of 73.75 kW kg⁻¹. Interestingly, the ASC also remains excellent cycling stability of 90.1% retention after 10 000 cycles at 10 A g⁻¹. This work provides a perspective for offsetting the drawbacks between the multi-metal sulfides and carbonaceous materials, which demonstrates great potential for future energy storage or conversion.

Declaration of Competing Interest

The authors declare that they have no known competing financial interests or personal relationships that could have appeared to influence the work reported in this paper.

Acknowledgements

The authors acknowledge the financial support from Natural Science Foundation of China (21671173, 11874390) and Zhejiang Provincial Ten Thousand Talent Program (2017R52043).

Appendix A. Supplementary data

Supplementary data to this article can be found online at <https://doi.org/10.1016/j.cej.2019.122544>.

References

- [1] K. Jayaramulu, D.P. Dubal, B. Nagar, V. Ranc, O. Tomanec, M. Petr, K.K.R. Datta, R. Zboril, P.G. Romero, R.A. Fischer, Ultrathin hierarchical porous carbon nanosheets for high-performance supercapacitors and redox electrolyte energy storage, *Adv. Mater.* 30 (2018) 1705789.
- [2] H. Liang, C. Xia, A.-H. Emwas, D.H. Anjum, X. Miao, H.N. Alshareef, Phosphine plasma activation of α -Fe₂O₃ for high energy asymmetric supercapacitors, *Nano Energy* 49 (2018) 155.
- [3] P. Simon, Y. Gogotsi, B. Dunn, Where do batteries end and supercapacitors begin? *Science* 343 (2014) 1210.
- [4] H.S. Chavan, B. Hou, A.T.A. Ahmed, Y. Jo, S. Cho, J. Kim, S.M. Pawar, S. Cha, A.I. Inamdar, H. Im, Nanoflake NiMoO₄ based smart supercapacitor for intelligent power balance monitoring, *Sol. Energy Mater. Sol. Cells* 185 (2018) 166.
- [5] A.I. Inamdar, J. Kim, Y. Jo, H. Woo, S. Cho, S.M. Pawar, S. Lee, J.L. Gunjaker, Y. Cho, B. Hou, S. Cha, J. Kwak, Y. Park, H. Kim, H. Im, Highly efficient electro-optimally tunable smart-supercapacitors using an oxygen-excess nanograin tungsten oxide thin film, *Sol. Energy Mater. Sol. Cells* 166 (2017) 78.
- [6] S. Sun, J. Luo, Y. Qian, Y. Jin, Y. Liu, Y. Qiu, X. Li, C. Fang, J. Han, Y. Huang, Metal-organic framework derived honeycomb Co₉S₈@C composites for high-performance supercapacitors, *Adv. Energy Mater.* 8 (2018) 1801080.
- [7] B.Y. Guan, A. Kushima, L. Yu, S. Li, J. Li, X.W. Lou, Coordination polymers derived general synthesis of multishelled mixed metal-oxide particles for hybrid supercapacitors, *Adv. Mater.* 29 (2017) 1605902.
- [8] L.F. Shen, L. Yu, H.B. Wu, X.Y. Yu, X.G. Zhang, X.W. Lou, Formation of nickel cobalt sulfide ball-in-ball hollow spheres with enhanced electrochemical pseudocapacitive properties, *Nat. Commun.* 6 (2015) 6694.
- [9] Y. Liu, Z.B. Wang, Y.J. Zhong, M. Tade, W. Zhou, Z.P. Shao, Molecular design of mesoporous NiCo₂O₄ and NiCo₂S₄ with sub-micrometer-polyhedron architectures for efficient pseudocapacitive energy storage, *Adv. Funct. Mater.* 27 (2017) 1701229.
- [10] Z. Li, D. Zhao, C. Xu, J. Ning, Y. Zhong, Z. Zhang, Y. Wang, Y. Hu, Reduced CoNi₂S₄ nanosheets with enhanced conductivity for high-performance supercapacitors, *Electrochim. Acta* 278 (2018) 33.
- [11] S.J. Peng, L.L. Li, H.T. Tan, R. Cai, W.H. Shi, C.C. Li, S. Mhaisalkar, M. Srinivasan, S. Ramakrishna, Q.Y. Yan, MS₂ (M = Co and Ni) hollow spheres with tunable interiors for high-performance supercapacitors and photovoltaics, *Adv. Funct. Mater.* 24 (2014) 2155.
- [12] L. Hou, Y. Shi, S. Zhu, M. Rehan, G. Pang, X. Zhang, C. Yuan, Hollow mesoporous hetero-NiCo₂S₄/Co₉S₈ submicro-spindles: unusual formation and excellent pseudocapacitance towards hybrid supercapacitors, *J. Mater. Chem. A* 5 (2017) 133.
- [13] X.Z. Song, F.F. Sun, Y.L. Meng, Z.W. Wang, Q.F. Su, Z. Tan, Hollow core-shell NiCo₂S₄@MoS₂ dodecahedrons with enhanced performance for supercapacitors and hydrogen evolution reaction, *New J. Chem.* 43 (2019) 3601.
- [14] Y. Jia, Y. Ma, Y. Lin, J. Tang, W. Shi, W. He, In-situ growth of hierarchical NiCo₂S₄/MoS₂ nanotube arrays with excellent electrochemical performance, *Electrochim. Acta* 289 (2018) 39.
- [15] J. Han, G. Xu, B. Ding, J. Pan, H. Dou, D.R. MacFarlane, Porous nitrogen-doped hollow carbon spheres derived from polyaniline for high performance supercapacitors, *J. Mater. Chem. A* 2 (2014) 5352.
- [16] J. Wang, H. Tang, H. Ren, R. Yu, J. Qi, D. Mao, H. Zhao, D. Wang, pH-regulated synthesis of multi-shelled manganese oxide hollow microspheres as supercapacitor electrodes using carbonaceous microspheres as templates, *Adv. Sci.* 1 (2014) 1400011.
- [17] M. Liu, X. Wang, D. Zhu, L. Li, H. Duan, Z. Xu, Z. Wang, L. Gan, Encapsulation of NiO nanoparticles in mesoporous carbon nanospheres for advanced energy storage, *Chem. Eng. J.* 308 (2017) 240.
- [18] L. Sheng, L. Jiang, T. Wei, Z. Liu, Z. Fan, Spatial charge storage within honeycomb-carbon frameworks for ultrafast supercapacitors with high energy and power densities, *Adv. Energy Mater.* (2017) 1700668.
- [19] C. Guan, X.M. Liu, W.N. Ren, X. Li, C.W. Cheng, J. Wang, Rational design of metal-organic framework derived hollow NiCo₂O₄ arrays for flexible supercapacitor and electrocatalysis, *Adv. Energy Mater.* 1602391 (2017).
- [20] Y.M. Chen, L. Yu, X.W. Lou, Hierarchical tubular structures composed of Co₃O₄ hollow nanoparticles and carbon nanotubes for lithium storage, *Angew. Chem. Int. Ed.* 55 (2016) 5990.
- [21] E. Hu, Y. Feng, J. Nai, D. Zhao, Y. Hu, X.W.D. Lou, Construction of hierarchical Ni-Co-P hollow nanobricks with oriented nanosheets for efficient overall water splitting, *Energy Environ. Sci.* 11 (2018) 872.
- [22] W. Lu, Z. Yuan, C. Xu, J. Ning, Y. Zhong, Z. Zhang, Y. Hu, Construction of mesoporous Cu-doped Co₉S₈ rectangular nanotube arrays for high energy density all-solid-state asymmetric supercapacitors, *J. Mater. Chem. A* 7 (2019) 5333.
- [23] Y. Feng, C. Xu, E. Hu, B. Xia, J. Ning, C. Zheng, Y. Zhong, Z. Zhang, Y. Hu, Construction of hierarchical FeP/Ni₂P hollow nanospindles for efficient oxygen evolution, *J. Mater. Chem. A* 6 (2018) 1410.
- [24] E. Hu, J. Ning, D. Zhao, C. Xu, Y. Lin, Y. Zhong, Z. Zhang, Y. Wang, Y. Hu, A room-temperature postsynthetic ligand exchange strategy to construct mesoporous Fe-doped CoP hollow triangle plate Arrays for efficient electrocatalytic water splitting, *Small* 14 (2018) 1704233.
- [25] G. Zhang, X.W.D. Lou, General synthesis of multi-shelled mixed metal oxide hollow spheres with superior lithium storage properties, *Angew. Chem. Int. Ed.* 53 (2014) 9041.
- [26] D. Wang, W. Zhu, Y. Yuan, G. Du, J. Zhu, X. Zhu, G. Pezzotti, Kelp-like structured NiCo₂S₄-C-MoS₂ composite electrodes for high performance supercapacitor, *J. Alloys Compd.* 735 (2018) 1505.
- [27] Y. Wang, L. Yu, X.W. Lou, Synthesis of highly uniform molybdenum-glycerate spheres and their conversion into hierarchical MoS₂ hollow nanospheres for lithium-ion batteries, *Angew. Chem. Int. Ed.* 55 (2016) 7423.
- [28] Y. Wang, L. Yu, X.W. Lou, Formation of triple-shelled molybdenum-polydopamine hollow spheres and their conversion into MoO₂/carbon composite hollow spheres for lithium-ion batteries, *Angew. Chem. Int. Ed.* 55 (2016) 14668.
- [29] G. Libo, S. Jian, S.J. Utama, C. Ke, H. Ying, S. Dong, T. Xiao-Ming, L. Yang, Graphene-bridged multifunctional flexible fiber supercapacitor with high energy density, *ACS Appl. Mater. Interfaces* 10 (2018) 28597.
- [30] X. Geng, Y. Zhang, Y. Han, J. Li, L. Yang, M. Benamara, L. Chen, H. Zhu, Two-Dimensional water-coupled metallic MoS₂ with nanochannels for ultrafast supercapacitors, *Nano Lett.* 17 (2017) 1825.
- [31] X. Geng, Y. Jiao, Y. Han, A. Mukhopadhyay, L. Yang, H. Zhu, Freestanding metallic

- 1T MoS₂ with dual ion diffusion paths as high rate anode for sodium-ion batteries, *Adv. Funct. Mater.* 27 (2017) 1702998.
- [32] L.Q. Li, H.B. Yang, J. Yang, L.P. Zhang, J.W. Miao, Y.F. Zhang, C.C. Sun, W. Huang, X.C. Dong, B. Liu, Hierarchical carbon@Ni₃S₂@MoS₂ double core-shell nanorods for high-performance supercapacitors, *J. Mater. Chem. A* 4 (2016) 1319.
- [33] C.J. Xuan, Z.K. Peng, K.D. Xia, J. Wang, W.P. Xiao, W. Lei, M.X. Gong, T. Huang, D.L. Wang, Self-supported ternary Ni-Fe-P nanosheets derived from metalorganic frameworks as efficient overall water splitting electrocatalysts, *Electrochim. Acta* 258 (2017) 423.
- [34] S. Gao, Y. Zhang, Y. Zhang, B. Wang, S. Yang, Modification of carbon nanotubes via birch reaction for enhanced her catalyst by constructing pearl necklace-like NiCo₂P₂-CNT composite, *Small* 14 (2018) 1804388.
- [35] G. Liu, J. Liu, W. Li, C. Liu, F. Wang, J. He, C. Guild, J. Jin, D. Kriz, R. Miao, S.L. Suib, Aerobic oxidation of alcohols over Ru-Mn-Ce and Ru-Co-Ce catalysts: the effect of calcination temperature, *Appl. Catal. A Gen.* 535 (2017) 77.
- [36] Y. Wang, T. Zhu, Y. Zhang, X. Kong, S. Liang, G. Cao, A. Pan, Rational design of multi-shelled CoO/Co₉S₈ hollow microspheres for high-performance hybrid supercapacitors, *J. Mater. Chem. A* 5 (2017) 18448.
- [37] K. Xiao, L. Zhou, M. Shao, M. Wei, Fabrication of (Ni, Co)_{0.85}Se nanosheet arrays derived from layered double hydroxides toward largely enhanced overall water splitting, *J. Mater. Chem. A* 6 (2018) 7585.
- [38] S. Kandula, K.R. Shrestha, N.H. Kim, J.H. Lee, Fabrication of a 3D hierarchical sandwich Co₉S₈/alpha-MnS@N-C@MoS₂ nanowire architectures as advanced electrode material for high performance hybrid supercapacitors, *Small* 14 (2018) 1800291.
- [39] X.Y. Yu, Y. Feng, Y. Jeon, B. Guan, X.W. Lou, U. Paik, Formation of Ni-Co-MoS₂ nanoboxes with enhanced electrocatalytic activity for hydrogen evolution, *Adv. Mater.* 28 (2016) 9006.
- [40] C. Xu, Z. Lin, D. Zhao, Y. Sun, Y. Zhong, J. Ning, C. Zheng, Z. Zhang, Y. Hu, Facile in situ fabrication of Co nanoparticles embedded in 3D N-enriched mesoporous carbon foam electrocatalyst with enhanced activity and stability toward oxygen reduction reaction, *J. Mater. Sci.* 54 (2019) 5412.
- [41] Q.L. Xu, C.J. Jiang, B.C. Cheng, J.G. Yu, Enhanced visible-light photocatalytic H₂-generation activity of carbon/g-C₃N₄ nanocomposites prepared by two-step thermal treatment, *Dalton Trans.* 46 (2017) 10611.
- [42] T.B. Schon, P.M. DiCarmine, D.S. Seferos, Polyfullerene electrodes for high power supercapacitors, *Adv. Energy Mater.* 4 (2014) 1301509.
- [43] W. Guo, Y. Li, Y. Tang, S. Chen, Z. Liu, L. Wang, Y. Zhao, F. Gao, TiO₂ nanowire arrays on titanium substrate as a novel binder-free negative electrode for asymmetric supercapacitor, *Electrochim. Acta* 229 (2017) 197.
- [44] H. Chen, Y. Qin, H. Cao, X. Song, C. Huang, H. Feng, X. Zhao, Synthesis of amorphous nickel-cobalt-manganese hydroxides for supercapacitor-battery hybrid energy storage system, *Energy Storage Mater.* 17 (2018) 194.
- [45] D. Sarkar, D. Das, S. Das, A. Kumar, S. Patil, K.K. Nanda, D. Sarma, A.K. Shukla, Expanding interlayer spacing in MoS₂ for realizing an advanced supercapacitor, *ACS Energy Lett.* 4 (2019) 1602.
- [46] D.K. Nandi, S. Sahoo, S. Sinha, S. Yeo, H. Kim, R.N. Bulakhe, J. Heo, J.-J. Shim, S.-H. Kim, Highly uniform atomic layer-deposited MoS₂@3D-Ni-foam: a novel approach to prepare an electrode for supercapacitors, *ACS Appl. Mater. Interfaces* 9 (2017) 40252.
- [47] W. Kong, C. Lu, W. Zhang, J. Pu, Z. Wang, Homogeneous core-shell NiCo₂S₄ nanostructures supported on nickel foam for supercapacitors, *J. Mater. Chem. A* 3 (2015) 12452.
- [48] S. Liu, Y. Yin, K.S. Hui, K.N. Hui, S.C. Lee, S.C. Jun, High-performance flexible quasi-solid-state supercapacitors realized by molybdenum dioxide@nitrogen-doped carbon and copper cobalt sulfide tubular nanostructures, *Adv. Sci.* 5 (2018) 1800733.
- [49] L. Fan, K. Lin, J. Wang, R. Ma, B. Lu, A nonaqueous potassium-based battery-supercapacitor hybrid device, *Adv. Mater.* 30 (2018) 1800804.
- [50] X. Wang, H. Li, H. Li, S. Lin, J. Bai, J. Dai, C. Liang, X. Zhu, Y. Sun, S. Dou, Heterostructures of Ni-Co-Al layered double hydroxide assembled on V₄C₃ MXene for high-energy hybrid supercapacitors, *J. Mater. Chem. A* 7 (2019) 2291.
- [51] Q. Xue, H. Gan, Y. Huang, M. Zhu, Z. Pei, H. Li, S. Deng, F. Liu, C. Zhi, Boron element nanowires electrode for supercapacitors, *Adv. Energy Mater.* (2018) 1703117.
- [52] E. Lim, C. Jo, H. Kim, M.H. Kim, Y. Mun, J. Chun, Y. Ye, J. Hwang, K.S. Ha, K.C. Roh, K. Kang, S. Yoon, J. Lee, Facile Synthesis of Nb₂O₅@carbon core-shell nanocrystals with controlled crystalline structure for high-power anodes in hybrid supercapacitors, *ACS Nano* 9 (2015) 7497.
- [53] S. Wang, Y. Shao, W. Liu, Y. Wu, X. Hao, Elastic sandwich-type GaN/MnO₂/MnON composites for flexible supercapacitors with high energy density, *J. Mater. Chem. A* 6 (2018) 13215.
- [54] Y. Li, H. Wang, L. Wang, Z. Mao, R. Wang, B. He, Y. Gong, X. Hu, Mesopore-induced ultrafast Na⁺-storage in T-Nb₂O₅/carbon nanofiber films toward flexible high-power Na-ion capacitors, *Small* 15 (2019) 1804539.
- [55] J. Tao, N. Liu, J. Rao, L. Ding, M.R.A. Bahrani, L. Li, J. Su, Y. Gao, Series asymmetric supercapacitors based on free-standing inner-connection electrodes for high energy density and high output voltage, *Nanoscale* 6 (2014) 15073.
- [56] W.H. Luo, G.F. Zhang, Y.X. Cui, Y. Sun, Q. Qin, J. Zhang, W.J. Zheng, One-step extended strategy for the ionic liquid-assisted synthesis of Ni₃S₄-MoS₂ heterojunction electrodes for supercapacitors, *J. Mater. Chem. A* 5 (2017) 11278.
- [57] X.J. Yang, L.J. Zhao, J.S. Lian, Arrays of hierarchical nickel sulfides/MoS₂ nanosheets supported on carbon nanotubes backbone as advanced anode materials for asymmetric supercapacitor, *J. Power Sour.* 343 (2017) 373.
- [58] Z. Li, Z. Qin, W. Zhang, Z. Li, Controlled synthesis of Ni(OH)₂/MoS₂ nanohybrids for high-performance supercapacitors, *Mater. Chem. Phys.* 209 (2018) 291.
- [59] L. Huang, H. Hou, B. Liu, K. Zeinu, X. Zhu, X. Yuan, X. He, L. Wu, J. Hu, J. Yang, Ultrahigh-performance pseudocapacitor based on phase-controlled synthesis of MoS₂ nanosheets decorated Ni₃S₂ hybrid structure through annealing treatment, *Appl. Surf. Sci.* 425 (2017) 879.
- [60] Y. Zhu, Z. Wu, M. Jing, X. Yang, W. Song, X. Ji, Mesoporous NiCo₂S₄ nanoparticles as high-performance electrode materials for supercapacitors, *J. Power Sour.* 273 (2015) 584.
- [61] J. Zhang, H.J. Feng, J.Q. Yang, Q. Qin, H.M. Fan, C.Y. Wei, W.J. Zheng, Solvothermal synthesis of three-dimensional hierarchical CuS microspheres from a Cu-based ionic liquid precursor for high-performance asymmetric supercapacitors, *ACS Appl. Mater. Interfaces* 7 (2015) 21735.
- [62] Q.T. Qu, L. Li, S. Tian, W.L. Guo, Y.P. Wu, R. Holze, A cheap asymmetric supercapacitor with high energy at high power: activated carbon//K_{0.27}MnO₂·0.6H₂O, *J. Power Sour.* 195 (2010) 2789.
- [63] M. Pang, G. Long, J. Shang, J. Yuan, H. Wei, B. Wang, X. Liu, Y. Xi, D. Wang, F. Xu, Ethanol-assisted solvothermal synthesis of porous nanostructured cobalt oxides (CoO/Co₃O₄) for high-performance supercapacitors, *Chem. Eng. J.* 280 (2015) 377.
- [64] P. Pazhamalai, K. Krishnamoorthy, S. Sahoo, V.K. Mariappan, Copper tungsten sulfide anchored on Ni-foam as a high-performance binder free negative electrode for asymmetric supercapacitor, *Chem. Eng. J.* 359 (2019) 409.
- [65] V.K. Mariappan, K. Krishnamoorthy, P. Pazhamalai, S. Sahoo, S.S. Nardekar, S.-J. Kim, Nanostructured ternary metal chalcogenide-based binder-free electrodes for high energy density asymmetric supercapacitors, *Nano Energy* 57 (2019) 307.
- [66] A.K. Das, R. Bera, A. Maitra, S.K. Karan, S. Paria, L. Halder, S.K. Si, A. Bera, B.B. Khouta, Fabrication of an advanced asymmetric supercapacitor based on a microcubical PB@MnO₂ hybrid and PANI/GNP composite with excellent electrochemical behavior, *J. Mater. Chem. A* 5 (2017) 22242.